RESEARCH ARTICLE

Structural insight into palladium-nickel clusters over mordenite zeolite for carbene-insertion reaction

Guangchao Li[1,2], Ping-Luen Baron Ho[2], Bryan Kit Yue Ng[2], Tai-Sing Wu[3], Pawel Rymarz[2], Shik Chi Edman Tsang (✉)[2]

1 Department of Applied Biology and Chemical Technology, The Hong Kong Polytechnic University, Hong Kong 999077, China
2 Department of Chemistry, University of Oxford, Oxford OX1 3QR, UK
3 Synchrotron Radiation Research Center, Hsinchu 30076, China

Abstract The advancement of heterogeneous catalysts incorporating metal clusters in the nanometric size range has garnered significant attention due to their extraordinary catalytic activity and selectivity. The detailed characterization and understanding of the atomic structure of these metal clusters within catalysts is crucial for elucidating the underlying reaction mechanisms. In the present study, a distinctive three-atom PdNi cluster, characterized by two Pd atoms at terminal positions and a central Ni atom, was synthesized over mordenite zeolite. The presence of atomic PdNi clusters within the eight-membered ring side pocket area was confirmed by multiple advanced analytical techniques, including magic-angle spinning nuclear magnetic resonance spectroscopy, synchrotron X-ray powder diffraction, extended X-ray absorption fine structure spectroscopy, and high-angle annular dark-field scanning transmission electron microscopy. The catalytic activity of the confined active species was examined by the carbene-mediated reactions of ethyl-2-diazoacetate to ethyl-2-methoxyacetate as a model reaction. Compared to the Pd-mordenite and Ni-mordenite, the PdNi-mordenite catalyst incorporates a PdNi cluster, which demonstrates a superior performance, achieving 100% conversion and high selectivity under the same reaction conditions. Our study elucidates the potential of constructing bimetallic clusters in zeolites, providing valuable insights for developing new heterogeneous catalysts applicable to a wide range of catalytic processes.

Keywords zeolite, metal cluster, synchrotron X-ray diffraction, carbene-mediated reaction

1 Introduction

Progress in the modern large-scale chemical industry hinges on the continued development of catalysts that reduce reaction conditions while enhancing selectivity and yields [1]. Carbene transfer reactions are often employed in small-scale organic molecule synthesis in the laboratory [2]. Besides, few suitable heterogeneous catalysts exist that promote this chemistry with high activity or enough selectivity. Ligand-supported clusters have been proven to be successful catalysts but often decompose under ligand exchange [1,3]. Therefore, the design and development of a recyclable heterogeneous catalyst is often sought after.

Solid-supported clusters are a promising, stable alternative in heterogeneous catalysis [4]. Among the various solid-supported materials, porous materials, including zeolites and metal-organic frameworks (MOFs), have attracted considerable attention. This is primarily due to wide-ranging applications across diverse fields, their cost-effectiveness, and their environmentally sustainable nature [5]. Zeolites possess unique pores, cages, and adsorption sites that facilitate the confined formation and stabilization of metal clusters. These characteristics, coupled with their well-defined structure, high thermal stability, and adjustable acidity, make metal-loaded zeolites promising catalysts for small-molecule chemistry [6].

Recent studies have demonstrated the effectiveness of planting ultrasmall metal clusters or single atoms embedded in zeolites as catalysts for various catalytic reactions [7]. For instance, Sun et al. [8] reported a

significant enhancement in the hydrogen generation of ammonia borane hydrolysis due to the synergetic effect of confined ultrasmall ruthenium clusters and zeolite frameworks. Similarly, Zhang et al. [9] developed a core-shell Pd@BEA catalyst with the Pd cluster inside the channel of Beta zeolite. This catalyst showed significantly enhanced performance in the hydrogenation of substituted nitroarenes into the corresponding anilines, owing to the sterically selective adsorption of the nitroarenes on the Pd nanoparticles controlled by the zeolite micropores. Furthermore, compared to a mono-metallic catalyst, bi-metallic catalysts have been found to exhibit more excellent stability, selectivity, and activity in reactions compared to their mono-metallic counterparts. Sun et al. [10] demonstrated that sub-nanometric hybrid bimetallic clusters of Pd-M(OH)$_2$, (M = Ni, Co) in zeolites can exhibit high catalytic activity in hydrogen generation from formic acid decomposition. In addition, Wun et al. [11] reported a simple method for assembling dual metal atoms within zeolitic micropores. Utilizing this protocol, Chen et al. [12] developed a Cu-Co dual-atom over hierarchical USY zeolite, which showed superior reactivity with over 80% isolated yields for efficient dehydrogenative cross-coupling of unprotected phenols with amine partners. Therefore, the unique properties of zeolites and their ability to host metal clusters make them an attractive platform for developing efficient catalysts.

This study focuses on the development of a multi-metallic zeolite-based catalyst designed explicitly for carbene reactions. A series of metal-doped mordenite (MOR) zeolite catalysts (with metals including Pd, Ni, Cu, Sm, and Pb) were prepared using an ion exchange approach. MOR zeolite was adopted due to its larger channels than the other common zeolite, such as ZSM-5. This larger pore size is anticipated to facilitate better penetration of relatively large organic groups, thereby enhancing the catalytic process. Among the synthesized catalysts, the PdNi-MOR catalyst demonstrated superior catalytic performance for the methanol insertion reaction with ethyl-2-diazoacetate (EDA). This outstanding performance, compared to other prepared metal-doped catalysts (Pd-MOR, Ni-MOR, PdCu-MOR, PdSm-MOR, PdPb-MOR), can be attributed to the atomic dispersity of the PdNi clusters and the strong synergetic effects they exhibit within the confined environment of the zeolite pores. To gain a deeper understanding of the catalyst's performance, we characterized the precise structure and position distribution of the atomic PdNi clusters by using magic-angle spinning (MAS) nuclear magnetic resonance spectroscopy (NMR), synchrotron X-ray powder diffraction, extended X-ray absorption fine structure (EXAFS) spectroscopy, and high-angle annular dark-field (HAADF) scanning transmission electron microscopy (STEM). This work not only contributes to the development of effective catalysts for carbene-mediated reactions but also paves the way for the exploration of a new class of catalysts.

2 Experimental

2.1 Chemicals

Pd(NO$_3$)$_2$·2H$_2$O, Ni(NO$_3$)$_2$·6H$_2$O, Sm(NO$_3$)$_2$·6H$_2$O, Cu(NO$_3$)$_2$·3H$_2$O, Pb(NO$_3$)$_2$, methanol, and EDA were purchased from Sigma-Aldrich. MOR zeolite (ammonium type) was purchased from Alfa Aesar.

2.2 Materials synthesis

Ammonium type MOR was first calcinated in the tube furnace under a flowing stream of dry air at 550 °C for 6 h to obtain the proton-type MOR zeolite. After that, the pre-calcinated MOR zeolite was mixed with the ion source solution for ion exchange. The samples were vigorously stirred for 6 h under 80 °C. The mixture was then centrifuged with deionized water and ethanol until the separated liquid tested neutral using pH paper before drying in an oven overnight under 80 °C. Finally, all samples were first calcined at 500 °C for 8 h under airflow, and then the catalysts were reduced under 5% H$_2$ in N$_2$ flow at 400 °C for 2 h.

2.3 Characterization

The X-ray diffraction (XRD) measurements were carried out at room temperature on a Bruker D8 ADVANCE using a Cu Kα radiation source (γ = 1.5406 Å) in the 2θ range of 5°–70° at 0.01145° increments with a 0.5-s step time.

EXAFS spectra for all the samples were recorded at the Pd K absorption edge, in fluorescence mode using a Lytle fluorescence detector, under reaction conditions, at beamline BL07A of the Taiwan light source at National Synchrotron Radiation Research Centre in Taiwan. A Si (111) double crystal monochromator was used to scan the photon energy. The energy resolution for the incident X-ray photons was estimated to be 2×10^{-4}. The Demeter software package (Athena and Artemis) was used for XAFS data analysis. To ascertain the reproducibility of the experimental data, at least two scan sets were collected and compared for each sample. The spectra were calibrated with Pd foil as a reference. The amplitude parameter was obtained from EXAFS data analysis of the Pd foil, which was used as a fixed input parameter in the data fitting to allow the refinement of the coordination number of the absorption element.

X-ray photoelectron spectroscopy (XPS) was performed on a Thermo Fisher Scientific NEXSA spectrometer. The samples were analyzed using a micro-focused mono-

chromatic Al X-ray source (72 W) over approximately 400 microns. Data were recorded at pass energies of 200 eV for survey scans and 50 eV for high-resolution scans with 1 and 0.1 eV step sizes, respectively.

Synchrotron XRD (SXRD) data were collected at BL02B2 in SPring-8 with a wavelength of 0.689556(1) Å (which is 18 keV) with a zero error of –0.00015 degrees. The detector was a MYTHEN 2D plate detector with two 300-s scans being summed. Samples were loaded into 0.7 mm capillaries. The data analysis was performed using the Rietveld method using TOPAS software (TOPAS-Academic V7).

Temperature programmed reduction (TPR) data were collected on Chem BET Pulsar TPR/TPD Automated Chemisorption Analyzer using hydrogen gas. Samples were heated to 800 °C with a rating of 5 °C·min^{-1}.

Elemental data from inductively coupled plasma mass spectrometry (ICP-MS) was collected on Elan DRC II (Perkin-Elmer SCIEX, Norwalk, CT, USA).

The N_2 adsorption-desorption study was conducted on a Micromeritics ASAP 2020 Plus analyzer at liquid nitrogen temperature (77 K). The samples were pre-treated at 673 K with pressure below 1.0×10^{-2} Pa overnight. The specific surface area was obtained using the Brunauer-Emmett-Teller (BET) equation, the micropore volume and micropore surface areas were calculated using a *t*-plot, and the pore size distribution was calculated using the Barrett-Joyner-Halenda model.

Conventional transmission electron microscopy and STEM images were performed at an accelerating voltage of 200 kV using JEOL JEM-2100 and ARM-F200 microscopes, respectively.

HAADF imaging with a probe current of 80 pA and a semi-convergence angle of 22 to 24 mrad is based on STEM.

MAS solid-state NMR (MAS SSNMR) experiments were recorded on a JEOL ECZ500R spectrometer with a 3.2- and 8-mm MAS probe. With resonance frequencies of 129.02 and 98.37 MHz for ^{27}Al and ^{29}Si nuclei, respectively. The single-pulse ^{27}Al MAS SSNMR spectra were collected using a 3.2-mm rotor at a spinning rate of 12 kHz with a recycle delay of 0.5 s and 1024 scans. A small flip angle ($\pi/12$) associated with a short pulse duration (0.16 μs) was used to ensure the homogeneous excitation of the whole signals to acquire a quantitative NMR spectrum. The chemical shifts of ^{27}Al were referenced to a 1.0-mol·L^{-1} aqueous $Al(NO_3)_3$ at 0 ppm. The single-pulse ^{29}Si MAS SSNMR spectra were acquired at a spinning rate of 4 kHz on an 8 mm probe head by a single $\pi/2$ pulse with 7.61 μs width and a recycle delay of 60 s and 24 scans. ^{29}Si chemical shifts were referenced to kaolinite at –91.5 ppm.

2.4 Catalytic performance

The catalyst (10 mg) under investigation was loaded into a 25-mL round bottom flask, and methanol (10 mL) under stirring. EDA (2 mL) was then added dropwise, and the flask was lowered into an oil bath. A reflux condenser was fitted to the top of the flask, and the reaction was left to occur. The experiment's length and the oil's temperature were changed multiple times. Once cooled and allowed the catalyst to settle, the liquid was decanted and analyzed by gas chromatography/mass spectrometry (GC-MS). The reaction conditions are 5 min of stirring the EDA and catalyst inside a 90-°C oil bath followed by adding the methanol before a 2-h reflux.

3   Results and discussion

3.1   Structural characterization

The structural characteristics of the MOR zeolites, both pre- and post-ion exchange treatment, were analyzed using laboratory XRD at first. As shown in Fig. 1(a), the pristine MOR, Pd-MOR, Ni-MOR, and PdNi-MOR all exhibit characteristic MOR structures without impurities. The absence of diffraction peaks corresponding to Pd, Ni, or their respective oxides suggests these species may be dispersed within the MOR zeolite or randomly distributed over the surface. In addition, the zeolite framework structures of different samples were studied by SSNMR. As shown in Fig. 1(b), ^{27}Al MAS SSNMR spectra of all samples have a sharp peak at 55 ppm, which can be attributed to the four-coordinate framework aluminum. A minor peak at 0 ppm, exclusive to the pristine MOR zeolite, is attributed to the extra-framework aluminum [13]. This peak has been eliminated from the MOR structure for samples of Pd-MOR, Ni-MOR, and PdNi-MOR, probably due to the extra-framework aluminum species being washed out during subsequent metal ion exchange treatments. Figure 1(c) presents the ^{29}Si single pulse MAS SSNMR spectra of pristine MOR, Pd-MOR, Ni-MOR, and PdNi-MOR. All samples show two prominent peaks located at –107 and –114 ppm. According to the previous literature, the peak at –107 ppm can be attributed to Q^3 (Si(OSi)$_3$(OAl)$_1$ or Si(OSi)$_3$OH), while the peak at –114 ppm can be attributed to Q^4 (Si(OSi)$_4$) [14]. Therefore, both the results from XRD and SSNMR suggest that the structure of zeolite is well maintained during the treatment of ion exchange.

The samples' porosity was characterized using nitrogen adsorption at 77 K. Figure 1(d) illustrates the corresponding adsorption and desorption isotherms. Each isotherm exhibits a sharp uptick in adsorption at low P/P_0 values and plateaus at higher pressures, closely aligning with a Type I isotherm according to the IUPAC classification. This suggests that the microporous structure of the MOR is well-preserved after the post-treatment. Additionally, the hysteresis loop observed in the P/P_0 region between
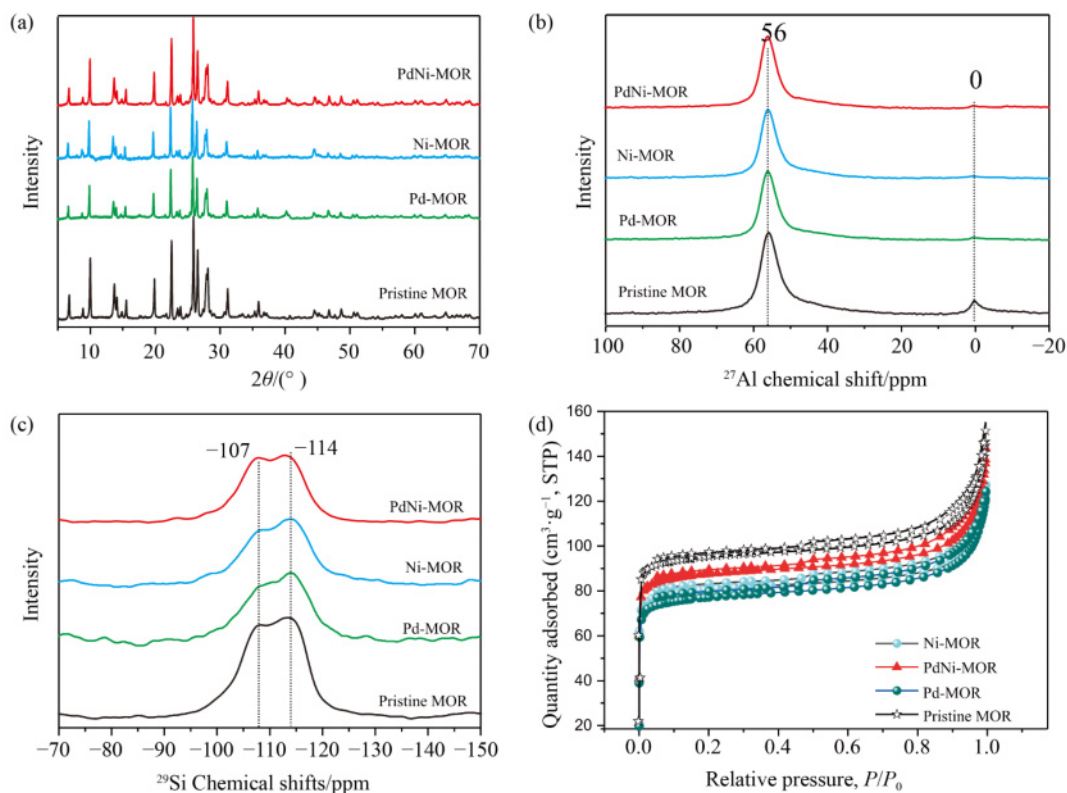
Fig. 1 (a) XRD patterns, (b) ^{27}Al, (c) ^{29}Si MAS SSNMR spectra, and (d) nitrogen adsorption-desorption isotherms of pristine MOR, Pd-MOR, Ni-MOR, and PdNi-MOR.

Table 1 Texture results of the samples from N$_2$ adsorption experiments and ICP-MS

Sample	S_{BET}a/(m^2·g^{-1})	S_{micro}/(m^2·g^{-1})	V_{micro}b/(cm^3·g^{-1})	Pore diameterc/Å	Theoretical valued		Experimental valuee	
					Pd/wt %	Ni/wt %	Pd/wt %	Ni/wt %
Pristine MOR	352.1	274.4	0.82	6.2	\	\	\	\
Pd-MOR	310.0	256.3	0.71	5.9	4	\	3.50	\
Ni-MOR	315.8	258.4	0.72	5.9	\	4	\	3.20
PdNi-MOR	324.5	260.4	0.75	6.0	2	2	1.79	0.86

a) Calculated by the BET equation; b) calculated by *t*-plot method; c) calculated from non-local density functional theory adsorption data; d) calculated by synthesis conditions of input metal source; e) calculated by ICP-MS.

0.4 and 1.0 is likely attributable to the filling of inter-crystalline spaces among relatively small MOR crystallites. The textural properties of the samples are summarized in Table 1. Pristine MOR has the largest microporous specific surface area of 352.1 m^2·g^{-1} with a pore diameter of 6.2 Å. Upon the introduction of metal species, a slight decrease in the microporous specific surface areas is observed, varying with different metal precursors. This can be attributed to the partial occupation of the micropore channels by the introduced metal species, which is also supported by the pore volume data in Table 1. The pristine MOR possesses the highest microporous volume of 0.82 cm^3·g^{-1} among the four samples, with Pd-MOR, Ni-MOR, and PdNi-MOR showing decreases of 0.11, 0.10, and 0.07 cm^3·g^{-1}, respectively. The precise metal content within the samples determined by ICP-MS is shown in Table 1. Compared to the theoretical input amounts of metal

sources in MOR for Pd-MOR, Ni-MOR, and PdNi-MOR, which were 4, 4, and 2–2 wt %, respectively, and thus the actual experimental contents were found to be 3.5, 3.2, and 1.79–0.86 wt %, respectively. These results suggest that Pd ions undergo ion exchange more readily than Ni ions in MOR zeolites probably due to the size and charge of Pd ions are more compatible with the MOR's structure. Previous literature reported that Pd^{2+} ions sited in side pockets are more stable than those in the main channels of MOR [15].

As shown in Fig. S1 (cf. Electronic Supplementary Material, ESM), the structural unit of MOR consists of 12-membered rings (12MR) with a pore size of approximately 6.5 Å × 7.0 Å, 8-membered rings (8MR) with a size of roughly 2.6 Å × 5.7 Å and 8MR side pockets measuring about 3.4 Å × 3.4 Å. Given the kinetic diameter of N$_2$ molecules (3.04 Å), BET N$_2$ adsorption can detect the 12MR channels and 8MR side pockets

within the framework. The observed changes in microporous specific surface area and volume suggest that the confined metal species, Pd and/or Ni, may be situated in the 12MR or 8MR side pocket. These confined metal species occupy a portion of the microporous space, thereby attenuating the adsorption of N_2 molecules in the microporous channels and resulting in a decrease in microporous volume and specific surface area.

Figure 2 presents the morphology and structure of the samples, namely, the bright-field TEM images for Pd-MOR, Ni-MOR, and HAADF-STEM for PdNi-MOR. Small Pd nanoparticles, estimated around 3.5 nm, are commonly observed throughout the Pd-MOR (Fig. 2(a)). In contrast, the Ni-MOR sample reveals the formation of larger Ni particles, approximately 6.3 nm in size, with a broad, non-uniform dispersion at a 100-nm scale (Fig. 2(b)). Interestingly, the co-introduction of Ni and Pd ions into MOR resulted in a high dispersion, with only non-occasionally a few large particles, potentially origina-

ting from Pd, Ni, or Pd-Cu clusters, detected on the outer surface of the same zeolite catalysts (Fig. 2(c)). This implies that most metal species are located within the MOR channel (Fig. 2(d)). Based on our understanding, the reason for the much smaller PdNi cluster size in the PdNi-MOR sample, compared to monometallic Pd-MOR or Ni-MOR, can be attributed to two main factors. Firstly, the synergistic interaction between Pd and Ni may inhibit their agglomeration [16,17]. Secondly, the co-ion exchange preparation method for PdNi-MOR, which uses a lower metal ion concentration than the monometallic samples (2 *vs*. 4 wt % shown in Table 1), could deter agglomeration, thus resulting in smaller PdNi clusters. These observations align with the XRD data (Fig. 1(a)) and BET results, which show that the microporous specific surface area for PdNi-MOR (260.4 $m^2 \cdot g^{-1}$) is largely maintained compared to the corresponding Pd-MOR (256.3 $m^2 \cdot g^{-1}$) and Ni-MOR (258.4 $m^2 \cdot g^{-1}$) samples.

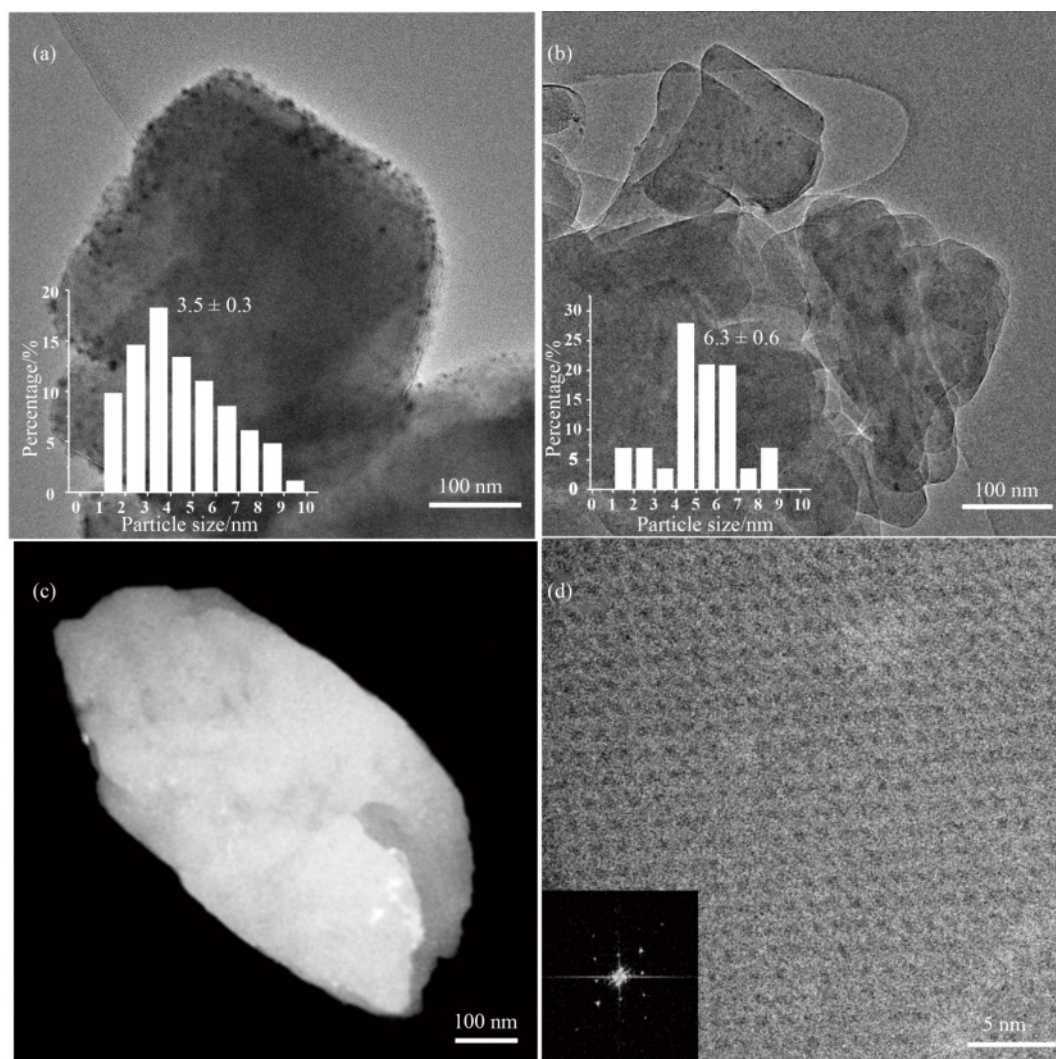To verify the simultaneous presence of both Pd and Ni

Fig. 2 Bright-field-TEM images of (a) Pd-MOR, (b) Ni-MOR, and HAADF-STEM of (c) PdNi/MOR, (d) with FFT along the [001] zone axis.
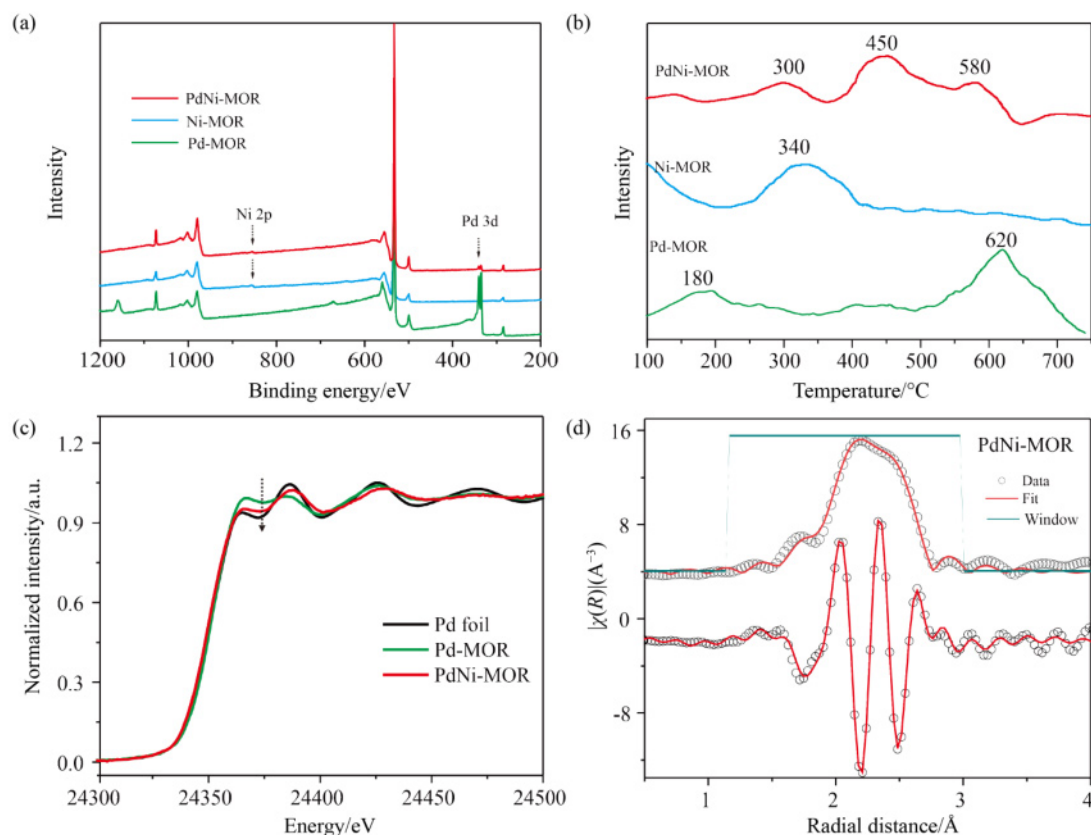
Fig. 3 (a) XPS survey spectrum, (b) H$_2$-TPR patterns of Pd-MOR, Ni-MOR, and PdNi-MOR, (c) normalized X-ray absorption near edge structure spectra at Pd K-edge of Pd foil, Pd-MOR, and PdNi-MOR, and (d) EXAFS fitting of PdNi-MOR with k2-weighted *q*-space with *R*-range at 1.35–3 Å.

metals in the prepared PdNi-MOR sample, XPS and H$_2$-TPR analyses were conducted. XPS survey spectra of Pd-MOR, Ni-MOR, and PdNi-MOR samples are shown in Fig. 3(a). The Pd 3d signal at approximately 335–340 eV in Pd-MOR and the Ni 2p signal at around 855–862 eV in Ni-MOR are evident. Both of these peaks are present in the PdNi-MOR sample, indicating the co-existence of Pd and Ni within the MOR structure. In addition, the Ni 2p XPS spectra for both Ni-MOR and PdNi-MOR are displayed in Fig. S2 (cf. ESM). Both metallic Ni (Ni^0) and divalent Ni (Ni^{2+}) were identified in the two samples. Meanwhile, compared to the sample of Ni-MOR, a notable shift of the primary peak corresponding to Ni^{2+}, toward a lower binding energy was observed in the PdNi-MOR sample. This shift is attributed to the mixing of relatively low energy metallic bands of Ni (3d) with high energy bands of Pd (4d), which allows electronic promotion from Pd to Ni in this metal cluster. Hence the result clearly suggests the presence of an electronic interaction between Pd and Ni in PdNi-MOR. Subsequently, H$_2$-TPR was performed to study the reduction behavior of the metal species supported over MOR (Fig. 3(b)). For the TPR reduction of Pd-MOR sample, a broad peak between 100 and 200 °C can be attributed to the reduction of Pd^{2+} to Pd^0 [18]. Meanwhile, a dominant peak with a reduction

temperature between 550 and 650 °C is also observed. Such high reduction temperature for the Pd-MOR sample is attributed to the presence of highly dispersed Pd species that strongly interact with the framework of MOR zeolite (i.e., MOR channels). For Ni-MOR, a strong and dominant peak is exhibited in between 280 and 380 °C, corresponding to the reduction temperature of Ni particles located on the external surface of zeolites [16]. In contrast, the PdNi-MOR sample displays multiple and broad hydrogen consumption peaks within the range of 300–650 °C, suggesting the presence of heterogeneous PdNi species within the MOR. Despite this, a shoulder peak with a reduction temperature around 300 °C corresponding to individual Ni species is still evident. The primary reduction temperatures are at 450 and 580 °C, which are much higher than those observed for Ni-MOR but still lower for Pd-MOR. It is worth noting that in bi-metallic supported catalysts, the less reducible component may stabilize the second metal in a highly dispersed state [17]. Therefore, the results suggest a potential electronic interaction between Ni and Pd, which influences the overall reduction temperature of PdNi-MOR. The ensemble effects between Pd and Ni in the PdNi-MOR sample are further characterized by X-ray absorption spectroscopy. As shown in Fig. 3(c), the oxidation state of Pd in PdNi-MOR is found to be lower than that in Pd-

MOR, indicating that the Pd atoms in PdNi-MOR are more electron-rich compared to those in Pd-MOR. Furthermore, the average local coordination environment of Pd species in both Pd foil and PdNi-MOR samples was investigated by EXAFS analysis (Figs. 3(d) and S3, cf. ESM). The quantitative results, like the average bond length (R) and the coordination number, which are derived from EXAFS data analysis, are summarized in Table 2. Only the first coordination sphere was fitted using a specific R-range for each studied standard, depending on the distance of the Pd-ligand path. Both Pd foil and PdNi-MOR samples show a Debye-Waller factor typical of well-ordered materials. For Pd foil, a characteristic coordination number of 12 is fixed according to the bulk value, and the Pd–Pd distance of 2.74 ± 0.01 Å was obtained, typical of noble metals arranged in the face central cubic local structure. In contrast, for the PdNi-MOR sample, the fitted results suggest a more complex coordination environment for the Pd species. Specifically, Pd appears to have three different types of neighboring atoms, resulting in three distinct bond lengths: Pd–Ni at 2.59 ± 0.01 Å, Pd–Pd at 2.69 ± 0.01 Å, and Pd–O$_{(framework)}$ at 2.73 ± 0.19 Å. Note that the longer-than-usual Pd–O distance reflects the long-range stabilization of the PdNi cluster by framework O rather than thermodynamic stable Pd–O bond formation. The total coordination number is approximately 12, similar to the Pd foil. However, the presence of Ni and O neighbors indicates the formation of a PdNi solid solution within the PdNi-MOR sample. This also suggests that the Pd and Ni atoms are not merely co-located within the zeolite but are integrated into a single, mixed-metal structure. This could have implications for the catalytic properties of the material.

3.2 Insight into the confined position of the metal cluster in MOR

The nature of the metal species in the MOR channel was characterized by the construction of the PdNi-MOR zeolite crystal structure based on the Rietveld refinement of high-resolution SXRD data [18−20]. The SXRD pattern was collected both for the pristine MOR and PdNi-MOR samples. The refined structures of pristine MOR and PdNi-MOR were obtained by the Rietveld method using TOPAS software (TOPAS-Academic V7). The fitted crystallographic parameters and atomic

information from the Rietveld refinement of the sample are shown in Tables S1, S2, and S3 (cf. ESM), respectively. In particular, a Fourier difference map, or a three-dimensional electron density difference map, was generated by comparing the electron density map of PdNi-MOR with that of pristine-MOR. The location of metal sites can hence be visualized, and Pd and Ni atoms were then added to the MOR zeolite model guided by the improved fitting parameters (Fig. 4(a)). The careful refined structure of the PdNi-MOR sample, which has refinement parameters within acceptable experimental errors, is shown in Fig. 4(b). A PdNi nanocluster, consisting of three atoms (two Pd on both sides and Ni in the middle), was indeed identified in the 8MR side pocket area, which is typically considered the reaction site [21−23]. The detailed local structure of the PdNi cluster is displayed in Figs. 4(c) and 4(d). The atomic configuration reveals that Pd1 and Pd2 atoms are coordinated to three oxygen sites: Pd1 to one O5 and two O7 sites and Pd2 to one O8 and two O3 sites. The bonding distances between oxygen and Pd atoms were as follows: Pd1–O5 and Pd1–O7 had bonding distances of 1.77(3) and 2.95(5) Å, respectively, while Pd2–O3 and Pd2–O8 had bonding distances of 2.32(1) and 1.93(4) Å, respectively. Additionally, the Ni atom is connected to two Pd atoms (Pd1 and Pd2) and four framework O sites (O3), with distances of 1.97(4), 2.47(1), and 3.40(8) Å for Ni–Pd1, Ni–Pd2, and Ni–O3, respectively. These connections and distances provide insight into the spatial arrangement of the atoms within the cluster. Furthermore, the angle between Pd1, Ni, and Pd2 was measured to be 115.78(8)°, indicating a unique spatial arrangement within the PdNi nanocluster/ alloy. This unique structure could potentially influence the catalytic properties of the nanocluster. It is worth noting that the synergistic effect between Pd and Ni has been identified as promising to form Pd-based alloys with improved catalytic behaviors [24−26].

3.3 Catalytic performance of carbene-mediated reaction over the developed catalyst

Inspired by previous work by Fortea-Pérez et al. [27], who reported the carbene-mediated reaction of diazoacetates over their developed Pd$_4$ cluster doped MOF catalysts, in our study, we then investigated the insertion of EDA into methanol as a model reaction. EDA was used as the carbene source due to its higher stability

Table 2 Structural parameters of PdNi-MOR were extracted from the EXAFS fitting for the Pd-centered scattering path with amplitude reduction factor at 0.65 and R-range at 1.35–3 Å

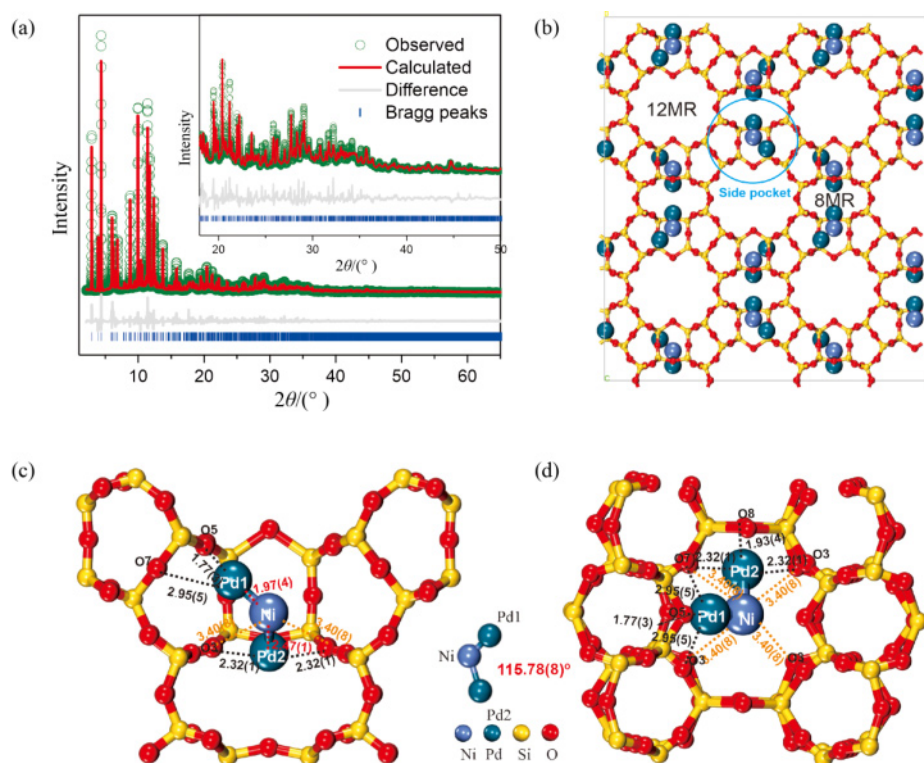| Sample	Scattering path	Bond length /Å	Coordination number	Debye-Waller factor/Å^2	ΔE/eV	R-factor/%
Pd foil	Pd−Pd	2.74 ± 0.01	12	0.005 ± 0.001	−0.63 ± 0.44	1.14
PdNi-MOR	Pd−Ni	2.59 ± 0.01	4.9 ± 1.5	0.007 ± 0.001		
	Pd−Pd	2.69 ± 0.01	5.6 ± 1.2	0.007 ± 0.001	−0.27 ± 0.64	0.65
	Pd−O$_{(framework)}$	2.73 ± 0.19	1.5 ± 0.4	0.007 ± 0.001		

Fig. 4 (a) Original and fitted SXRD patterns of PdNi-MOR sample, (b) distribution of PdNi cluster inside the 8MR side pocket of MOR based on the refined structure, the enlarged part of PdNi cluster is plotted both in (c) and (d) from different view directions.

compared to other diazo compounds, in addition to its ready availability and ease of storage. The alcohol insertion reaction was selected due to its reliance on smaller molecules, which are anticipated to penetrate the zeolite structure more effectively. The reaction details can be found in section two of the experimental part.

Table 3 summarizes the catalytic performance of various Pd catalysts in the EDA insertion reaction. Ideally, the desired product of the reaction is ethyl-2-methoxy acetate (EMA), although some side products may also occur due to side reactions. The identified side products from the GC-MS include ethyl-2-hydroxyacetate, diethyl succinate, diethyl fumarate, and diethyl maleate. As shown in Table 3, the Ni-MOR sample achieved a conversion of EDA of 58.6%, with the EMA and side products abundance at 54.0% and 4.6%, respectively. This suggests that Ni catalyst offers superior selectivity, but its catalytic activity is comparatively lower. In contrast, the Pd-MOR catalyst demonstrated high reactivity, achieving a 100% conversion within a 2-h reaction period. However, it also generated a significant quantity of by-products, accounting for 58.6% of the total product. The PdNi-MOR sample, on the other hand, combined the high activity of Pd with the selectivity of Ni, led to a greater consumption of EDA and a higher selectivity toward the desired product. Specifically, the conversion and EMA abundance in the products were 100% and 74.7%, respectively. Furthermore, we prepared a series of Pd-based MOR catalysts doped with

Table 3 Catalytic activities of different catalysts[a]

Entry	Catalyst	Conversion/%	EMA abundance/%	Side products/%
1	Ni-MOR	58.6	54.0	4.6
2	Pd-MOR	100	41.4	58.6
3	PdNi-MOR	100	74.7	25.3
4	PdSm-MOR	100	43.8	55.3
5	PdCu-MOR	100	45.8	53.1
6	PdPb-MOR	100	11.3	88.1

a) Reaction conditions: catalyst (10 mg) in the methanol (10 mL) with EDA (2 mL) at reflux temperature (90 °C) for 2 h. Products were analyzed by ^{1}H liquid NMR and GC-MS. The uncertainty in each value is ±5%.

various additional elements, including PbSm-MOR, PdCu-MOR, and PdPb-MOR. All these catalysts demonstrated high reactivity, but their selectivity was notably diminished.

3.4 Elucidation of reaction mechanism

To elucidate the observed reaction outcomes, it is crucial to propose mechanistic pathways that could account for the variations in the resultant products. The reaction

involves two steps: one is the formation of a carbenoid, and the other one is the methanol insertion; according to the previous iteration, the process of carbenoid formation has been extensively documented in the scientific literature [28]. The second step related to the canonical mechanism of alcohol insertion into a carbenoid over a singular metal site is well-established (Fig. S4, cf. ESM), often exemplified with Rh catalysts [29]. However, in this context, the metals within the clusters can be conceptualized as individual sites, with each atom performing a unique role in the reaction. This is analogous to Rh−Rh complexes, where one Rh atom serves as the binding site and the other acts as an electron sink.

Our study's catalytic data (Table 3) demonstrates a preference for either enhanced EMA (methanol insertion) selectivity or/and diethyl fumarate diethyl maleate (dimerization) selectivity. A pronounced selectivity toward EMA is discerned for NiPd-MOR catalyst, whereas catalysts such as PdSm-MOR, PdCu-MOR, and PbPd-MOR exhibit a preference for dimerization; this clearly suggests a potential synergistic interplay between the two metals within the catalysts. The observed high reactivity and selectivity are attributed to the formation of a Pd−Ni agglomerated cluster. The net electron transfer from Pd to Ni increases the electron affinity of Pd, thereby enhancing methanol adsorption. The central atom in the Ni cluster within the PdNi-MOR sample can then serve as an electron sink due to the shifts of d electrons from Pd into the interface of Pd−Ni alloy, effectively counterbalancing the dipole created by M-alcohol bonding. Based on this hypothesis, a 5-membered transition state mechanism is depicted in Scheme 1. Carbenoid formation is therefore taken place on the O5 oxygen-bound Pd due to its proximity to the zeolite's primary channel, while methanol is thus added at the more acidic Pd, proximal to the O8 oxygen according to

our refinement data. The metal atoms, confined within the zeolite structure, display an angle of 115.78(8)° for stereospecific methanol insertion reaction, which is slightly greater than the internal angle of a regular pentagon (108°). The substantial size of these metallic atoms can thus facilitate the exciting reaction. An anticipated synergistic effect between the two different metal atoms in the confined zeolitic space for the cooperative catalysis is therefore illustrated.

4 Conclusions

A series of metal-exchanged zeolites, both unimetallic and bimetallic, were synthesized by ion exchange. These zeolite catalysts were evaluated regarding their catalytic performance for a carbene-mediated insertion of an alcohol into a diazoacetate. These assessments concluded that various bimetallic clusters exhibit varying selectivity and activities during the reaction. Notably, PdNi clusters over MOR zeolite were found to be effective catalysts for the reaction. In contrast, PdSm, PdCu, or PdPb demonstrated selectivity toward specific side products, indicating the potential for targeted catalysis based on the choice of metal clusters.
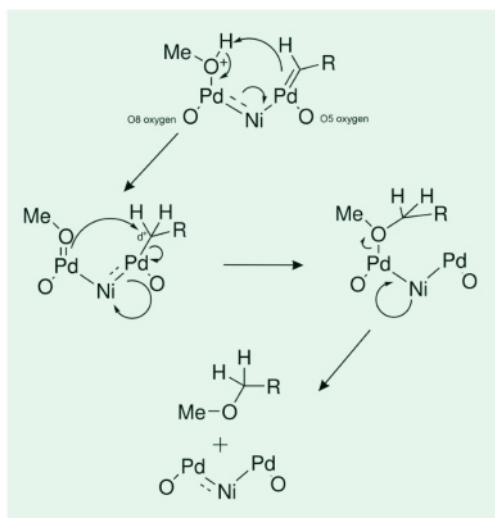
In the case of the PdNi-MOR sample, a unique three-atom cluster was discerned, with terminal, oxygen bound, Pd ions, and Ni occupying the middle position. This configuration offers rationalization for the observed catalytic activity and selectivity. Attempts to discern the mechanism and nature of the cluster's activity have been proposed based on EXAFS and SXRD results. The experimental data obtained support the predicted mechanism. Our work has made significant strides in demonstrating the effectiveness of zeolite-based bimetallic clusters as catalysts. We have shown that these catalysts can play a pivotal role in carbenoid chemistry, opening new avenues for further research and potential industrial applications.

Scheme 1 Proposed mechanism carbene-mediated reaction over Pd−Ni cluster in MOR.

References

1. Arakawa H, Aresta M, Armor J N, Barteau M A, Beckman E J, Bell A T, Bercaw J E, Creutz C, Dinjus E, Dixon D A, et al. Catalysis research of relevance to carbon management: progress, challenges, and opportunities. Chemical Reviews, 2001, 101(4): 953–996

2. Xia Y, Qiu D, Wang J. Transition-metal-catalyzed cross-couplings through carbene migratory insertion. Chemical Reviews, 2017, 117(23): 13810–13889

3. Su H L, Pérez L M, Lee S J, Reibenspies J H, Bazzi H S, Bergbreiter D E. Studies of ligand exchange in N-heterocyclic carbene silver(I) complexes. Organometallics, 2012, 31(10): 4063–4071

4. Li C, Liu Y. Bridging Heterogeneous and Homogeneous Catalysis: Concepts, Strategies, and Applications. New Jersey: John Wiley & Sons, 2014

5. Wang N, Sun Q, Yu J. Ultrasmall metal nanoparticles confined within crystalline nanoporous materials: a fascinating class of nanocatalysts. Advanced Materials, 2019, 31(1): e1803966

6. Chai Y, Shang W, Li W, Wu G, Dai W, Guan N, Li L. Noble metal particles confined in zeolites: synthesis, characterization, and applications. Advanced Science, 2019, 6(16): 1900299

7. Campbell C T, Parker S C, Starr D E. The effect of size-dependent nanoparticle energetics on catalyst sintering. Science, 2002, 298(5594): 811–814

8. Sun Q, Wang N, Bai R, Hui Y, Zhang T, Do D A, Zhang P, Song L, Miao S, Yu J. Synergetic effect of ultrasmall metal clusters and zeolites promoting hydrogen generation. Advanced Science, 2019, 6(10): 1802350

9. Zhang J, Wang L, Shao Y, Wang Y, Gates B C, Xiao F S A. Pd@zeolite catalyst for nitroarene hydrogenation with high product selectivity by sterically controlled adsorption in the zeolite micropores. Angewandte Chemie International Edition, 2017, 56(33): 9747–9751

10. Sun Q, Wang N, Bing Q, Si R, Liu J, Bai R, Zhang P, Jia M, Yu J. Subnanometric hybrid Pd-M(OH)$_2$, M = Ni, Co, clusters in zeolites as highly efficient nanocatalysts for hydrogen generation. Chem, 2017, 3(3): 477–493

11. Wun C K T, Mok H K, Chen T, Wu T S, Taniya K, Nakagawa K, Day S, Tang C C, Huang Z, Su H, et al. Atomically dispersed 3d metal bimetallic dual-atom catalysts and classification of the structural descriptors. Chem Catalysis, 2022, 2(9): 2346–2363

12. Chen T, Yu W, Wun C K T, Wu T S, Sun M, Day S, Li Z, Yuan B, Wang Y, Li M, et al. Cu−Co dual-atom catalysts supported on hierarchical USY zeolites for an efficient cross-dehydrogenative C(sp$_2$)-N coupling reaction. Journal of the American Chemical Society, 2023, 145(15): 8464–8473

13. Yu Z, Zheng A, Wang Q, Chen L, Xu J, Amoureux J P, Deng F. Insights into the dealumination of zeolite HY revealed by sensitivity-enhanced ^{27}Al DQ-MAS NMR spectroscopy at high field. Angewandte Chemie International Edition, 2010, 49(46): 8657–8661

14. Xu J, Wang Q, Li S, Deng F. Solid-State NMR in Zeolite Catalysis. Berlin: Springer, 2019

15. Satsuma A, Sahashi Y, Shibata J, Nishi K, Satokawa S, Itabashi K, Komai S, Yoshida H, Hattori T. Stability of Pd(II) ion in side pockets of mordenite under hydrothermal conditions. Microporous and Mesoporous Materials, 2005, 81(1-3): 135–138

16. Quindimil A, De-La-Torre U, Pereda-Ayo B, González-Marcos J A, González-Velasco J R. Ni catalysts with La as promoter supported over Y- and BETA- zeolites for CO$_2$ methanation. Applied Catalysis B: Environmental, 2018, 238: 393–403

17. Guczi L, Boskovic G, Kiss E. Bimetallic cobalt based catalysts. Catalysis Reviews. Science and Engineering, 2010, 52(2): 133–203

18. Leung K C, Hong S, Li G, Xing Y, Ng B K Y, Ho P L, Ye D, Zhao P, Tan E, Safonova O, et al. Confined Ru sites in a 13X zeolite for ultrahigh H$_2$ production from NH$_3$ decomposition. Journal of the American Chemical Society, 2023, 145(26): 14548–14561

19. Li G, Yoskamtorn T, Chen W, Foo C, Zheng J, Tang C, Day S, Zheng A, Li M M, Tsang S C E. Thermal alteration in adsorption sites over SAPO-34 zeolite. Angewandte Chemie International Edition, 2022, 61(27): e202204500

20. Li G, Foo C, Yi X, Chen W, Zhao P, Gao P, Yoskamtorn T, Xiao Y, Day S, Tang C C, et al. Induced active sites by adsorbate in zeotype materials. Journal of the American Chemical Society, 2021, 143(23): 8761–8771

21. Boronat M, Martínez-Sánchez C, Law D, Corma A. Enzyme-like specificity in zeolites: a unique site position in mordenite for selective carbonylation of methanol and dimethyl ether with CO. Journal of the American Chemical Society, 2008, 130(48): 16316–16323

22. Liu R, Fan B, Zhang W, Wang L, Qi L, Wang Y, Xu S, Yu Z, Wei Y, Liu Z. Increasing the number of aluminum atoms in T3 sites of a mordenite zeolite by low-pressure SiCl$_4$ treatment to catalyze dimethyl ether carbonylation. Angewandte Chemie International Edition, 2022, 61(18): e202116990

23. Liu Z, Yi X, Wang G, Tang X, Li G, Huang L, Zheng A. Roles of 8-ring and 12-ring channels in mordenite for carbonylation reaction: from the perspective of molecular adsorption and diffusion. Journal of Catalysis, 2019, 369: 335–344

24. Liu Z, Yang X, Cui L, Shi Z, Lu B, Guo X, Zhang J, Xu L, Tang Y, Xiang Y. High-performance oxygen reduction electrocatalysis enabled by 3D PdNi nanocorals with hierarchical porosity. Particle & Particle Systems Characterization, 2018, 35(5): 1700366

25. Sahoo L, Garg R, Kaur K, Vinod C, Gautam U K. Ultrathin twisty PdNi alloy nanowires as highly active ORR electrocatalysts exhibiting morphology-induced durability over 200 K cycles. Nano Letters, 2022, 22(1): 246–254

26. Wang T, Chutia A, Brett D J, Shearing P R, He G, Chai G, Parkin I P. Palladium alloys used as electrocatalysts for the oxygen reduction reaction. Energy & Environmental Science, 2021, 14(5): 2639–2669

27. Fortea-Pérez F R, Mon M, Ferrando-Soria J, Boronat M, Leyva-Perez A, Corma A, Herrera J M, Osadchii D, Gascon J, Armentano D, et al. The MOF-driven synthesis of supported palladium clusters with catalytic activity for carbene-mediated chemistry. Nature Materials, 2017, 16(7): 760–766

28. Padwa A, Weingarten M D. Cascade processes of metallo carbenoids. Chemical Reviews, 1996, 96(1): 223–270

29. Nakamura E, Yoshikai N, Yamanaka M. Mechanism of C–H bond activation/C–C bond formation reaction between diazo compound and alkane catalyzed by dirhodium tetracarboxylate. Journal of the American Chemical Society, 2002, 124(24): 7181–7192